

Sulfate reduction rates in the sediments of the Mediterranean continental shelf inferred from combined dissolved inorganic carbon and total alkalinity profiles

Eyal Wurgaft^{a,*,1}, Alyssa J. Findlay^{a,2}, Hanni Vigderovich^a, Barak Herut^{b,c}, Orit Sivan^a

^a The Department of Geological and Environmental Sciences, Ben-Gurion University of the Negev, Beer-Sheva, Israel

^b Israel Oceanographic and Limnological Research, Haifa, Israel

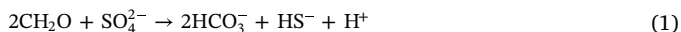
^c Department of Marine Geosciences, Leon H. Charney School of Marine Sciences, University of Haifa, Haifa, Israel

ABSTRACT

Microbial sulfate reduction in marine sediments is coupled either to anaerobic oxidation of methane (S-AOM) or organic material (organoclastic sulfate reduction, OSR). These two pathways of sulfate reduction are important components of the geochemical cycles of both sulfur and carbon in marine systems because they change the redox state of both elements and increase the dissolved inorganic carbon (DIC) and total alkalinity (TA) concentrations in sediment pore water. Here, we determine reaction rates of OSR and S-AOM in the sulfate methane transition zone (SMTZ) of the sediment based upon the different effect of each process on DIC and TA. Although TA has been used as a diagnostic proxy for the identification and determination of the governing chemical processes in numerous previous studies, we show that it can also be applied to disentangle and quantify net sulfate reduction rates in the SMTZ, provided that OSR and S-AOM are the principal processes that affect DIC and TA, and that the effects of other processes, such as carbonate mineral precipitation, are quantified by additional data. By integrating the obtained rates, we determine the contribution of each pathway to the total sulfate reduction. Calculated results from pore water profiles from the Southeastern Mediterranean continental shelf indicate that within the SMTZ, located at a depth of approximately 1 m, each pathway accounted for about half of the total sulfate reduction. The calculated OSR and S-AOM rates were similar to estimations of sulfate reduction rates based upon pore water sulfate profiles from studies in other sedimentary systems, in spite of the differences between these environments and the Southeastern Mediterranean continental shelf, showing that TA and DIC are a robust method for calculating net sulfate reduction. Furthermore, we show here that TA considerations can be used to quantitatively constrain the fractions of reduced sulfate that eventually precipitates as pyrite and FeS, versus the fraction that is oxidized and precipitates as elemental sulfur.

1. Introduction

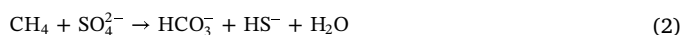
The oxidation of organic material in marine sediments is driven by the microbial reduction of a suite of electron acceptors, ranging from oxygen near the sediment-water interface to sulfate in the deeper parts of the sediments. When sulfate is depleted, the oxidation of organic material continues through fermentation and methanogenesis (Emerson et al., 1980; Froelich et al., 1979). The oxidation of organic material by sulfate reduction (organoclastic sulfate reduction, OSR) follows the generalized reaction:



where CH_2O represents organic material in which the oxidation state of the carbon is 0, which represents the mean of a variety of organic compounds (Arndt et al., 2013). Sulfate is readily available as a terminal electron acceptor for organic material reduction in marine systems,

due to its high concentration in seawater (28 mM), making OSR a quantitatively important remineralization processes, despite its lower energy yield relative to other electron acceptors (Froelich et al., 1979; Jørgensen, 1982). OSR is particularly important in locations where the burial rate of organic matter is high enough to allow significant portions of labile organic material to escape oxidation by other electron acceptors (Jørgensen and Kasten, 2006).

An additional pathway for microbial sulfate reduction is by anaerobic oxidation of methane (S-AOM) (Barnes and Goldberg, 1976; Martens and Berner, 1977; Reeburgh, 1976, 2007). This process follows the generalized reaction:



The concurrent consumption of sulfate and methane results in a distinctive Sulfate-Methane Transition Zone (SMTZ), in which sulfate and methane show opposing vertical gradients (e.g. Blair and Aller,

* Corresponding author.

E-mail address: ewurgaft@whoi.edu (E. Wurgaft).

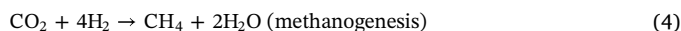
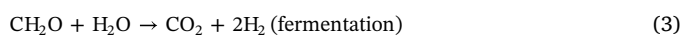
¹ Current address: The Department of Marine Chemistry and Geochemistry, Woods-Hole Oceanographic Institution, 360 Woods-Hole Road, Woods-Hole, MA 02543, USA.

² Current address: The Center for Geomicrobiology, Department of Biological Sciences, Aarhus University, 8000 Aarhus C, Denmark.

1995; Borowski et al., 1996; Iversen and Jørgensen, 1985; Reeburgh, 1976; Sansone and Martens, 1981). Due to the required presence of methane, S-AOM is limited to the SMTZ, whereas OSR can occur above, within and below the SMTZ (Berelson et al., 2005; Holmkvist et al., 2011; Komada et al., 2016; Treude et al., 2014; Treude et al., 2005). Notably, the vertical distribution of each pathway along the sediment column is also determined by the reactivity of the organic material in the sediment (Meister et al., 2013).

The reduction of sulfate in marine sediments by both OSR and S-AOM results in the subsequent precipitation and burial of H₂S in iron minerals, primarily pyrite (FeS₂), which is the main sink for sulfur in the ocean (Berner, 1982; Fike et al., 2015; Jørgensen and Kasten, 2006), and these processes thus play a major role in the global sulfur cycle. Furthermore, S-AOM is a critical pathway for methane consumption, which effectively prevents the release of most methane produced in marine sediments to the ocean and atmosphere (Reeburgh, 2007; Valentine, 2002). However, the geochemical implications of sulfate reduction are not restricted to the cycling of sulfur and organic carbon. Both S-AOM and OSR produce HCO₃⁻, thus increasing the dissolved inorganic carbon (DIC) and total alkalinity (TA) concentrations in the pore water. In turn, the increase in DIC and TA increases the saturation level of carbonate minerals, which often results in the precipitation of authigenic carbonates from the pore water (Gieskes et al., 2005; Jørgensen, 1992; Magalhães et al., 2012). Sun and Turchyn (2014) estimated that the authigenic precipitation of carbonate minerals accounts for at least 10% of the annual CaCO₃ accumulation in marine sediments, making it an important sink for both carbon and calcium. Finally, as the sulfide produced by OSR and S-AOM (Eqs. (1) and (2)) may interact with iron minerals such as oxides, carbonates, and phosphates, these sulfate reduction pathways also affect the oceanic cycling of iron and phosphorus (Egger et al., 2016; Hsu et al., 2014; Jørgensen et al., 2004; März et al., 2008, 2018; Neretin et al., 2004). Considering the diversity of processes and element cycles that interact, the mechanistic and quantitative understanding of the processes occurring in sediments in which both OSR and S-AOM take place is biogeochemically important, yet highly challenging. In particular, disentangling the relative contribution of S-AOM and OSR to sulfate reduction, their vertical distribution along the sediment column, and their reaction rates is impeded by the fact that both pathways use sulfate as a reactant and release the same products (sulfide and bicarbonate). The reactants specific to each process do not mitigate this problem, since methane measurements in sediment pore water are often inaccurate due to degassing during sampling (e.g. Wallace et al. (2000)). Furthermore, although the abundance of organic material in marine sediments and OSR rates are well correlated (Jørgensen and Kasten, 2006), this correlation cannot be used as an explicit indicator for OSR rates. Two main approaches have been used to differentiate S-AOM from OSR in marine sediment: (1) Experimental measurement of S-AOM and OSR rates using radioactive tracers (Fossing and Jørgensen, 1989; Roy et al., 2014; Treude et al., 2003, 2005, 2014; Treude et al., 2005) and (2) model calculations based on measured geochemical pore water data (Aharon and Fu, 2000; Antler et al., 2014, 2015; Berelson et al., 2005; Borowski et al., 2000; Fossing and Jørgensen, 1989; Reeburgh, 1976; Roy et al., 2014; Treude et al., 2003, 2005, 2014). Komada et al. (2016) extended this approach to include DIC, organic material and methane fluxes, as well as their ¹³C and ¹⁴C isotopic composition. This approach usually relies on Fick's law to derive flux balances for specific regions in the sediment column, such as the SMTZ (e.g. (Berelson et al., 2005; Borowski et al., 1996; Burdige and Komada, 2011; Komada et al., 2016; Niewohner et al., 1998; Reeburgh, 1976; Snyder et al., 2007)). Alternatively, the second derivative of concentration with depth can be used to calculate the reaction rates (e.g. (Fossing et al., 2000; Jørgensen and Parkes, 2010; Pastor et al., 2017; Sivan et al., 2007)). The second derivative of the concentration provides additional information about the distribution of the reaction rates along the sediment column, whereas flux estimations average certain regions of the sediment (e.g. the SMTZ)

and assume linearity along the concentration gradients. However, calculations based on the second derivative require a continuous concentration profile and the chemical data are usually discrete. Consequently, the usage of a smoothing algorithm is necessary, which in turn affects the accuracy of the obtained profiles (Lettmann et al., 2012). This choice between using flux-balance calculations (first derivative) and reaction rate profiles (second derivative) is particularly important to the determination of the relative contribution of S-AOM and OSR to the net sulfate reduction and/or DIC production in the SMTZ, because co-existing processes in averaged regions of the sediment column may complicate the interpretation of the results. For example, the production of methane in marine sediments usually follows Eqs. (3) and (4):



Burdige and Komada (2011) showed that if the methane that is produced within the sediment column by Eqs. (3) and (4) is recycled by S-AOM (Eq. (2)), the net stoichiometry in terms of sulfur, DIC and TA is identical to that of OSR (Eq. (1)). In this case, relying on the sulfate and/or DIC fluxes to the SMTZ may underestimate the contribution of S-AOM to sulfate reduction (or DIC production) in the SMTZ. This problem can be mitigated by calculating the specific reaction rate profiles of methanogenesis, S-AOM and OSR, provided that sufficient data are available.

Notably, when profile-based sulfate reduction rates are compared to radiotracer incubation rates (e.g. (Fossing et al., 2000; Iversen and Jørgensen, 1985; Jørgensen and Kasten, 2006; Jørgensen and Parkes, 2010; Treude et al., 2003; Treude et al., 2014; Treude et al., 2005)), the former tend to be lower. This discrepancy was suggested to be caused by the key difference that sulfate profiles represent the net sulfate consumption rates and estimates from the radiotracer incubations are closer to the gross rates (Jørgensen and Kasten, 2006; Jørgensen and Parkes, 2010; Jørgensen et al., 2001).

Since TA is affected by OSR and S-AOM (Eqs. (1) and (2)), it can be used as a proxy for these processes. This has been recognized and applied in numerous studies in the past with respect to sulfate reduction processes (Berner et al., 1970; Kastner et al., 2008; Pohlman et al., 2008; Sholkovitz, 1973; Snyder et al., 2007), as well as to other processes such as silicate weathering (Kim et al., 2016; Scholz et al., 2013; Wallmann et al., 2008) and iron and manganese reduction (Aller et al., 1986; Aller and Rude, 1988). However, in all of these studies, TA has been used as a diagnostic proxy, which serves mainly to distinguish between different processes based on their stoichiometry, rather than as a quantitative proxy. To the best of our knowledge, TA has not been used quantitatively for the determination of sulfate reduction rate profiles to date. Here, we show that TA can be used for such a quantitative measurement and estimate the rates of sulfate reduction by OSR and by S-AOM based on TA and DIC profiles, using the different effects of each process on DIC and TA per mol sulfate reduced ($\frac{\partial \text{DIC}}{\partial \text{SO}_4}$ and $\frac{\partial \text{TA}}{\partial \text{SO}_4}$, respectively).

2. Methods

2.1. Sampling

Sediment cores were collected from the Southeastern Mediterranean continental shelf during two research cruises conducted in September 2015 and January 2017 from sampling station SG1 (32°57'83 N, 34°55'29E; Fig. 1). The station is located at water depth approximately 85m and the bottom seawater temperature was about 16 °C. It was chosen for this study because high levels of methane and distinctive SMTZ has been previously observed in the upper few meters of the sediment (Sela-Adler et al., 2015). Notably, we define the SMTZ as the region of the sediment in which pore water sulfate and methane concentrations have opposite gradients. The sediment cores, which

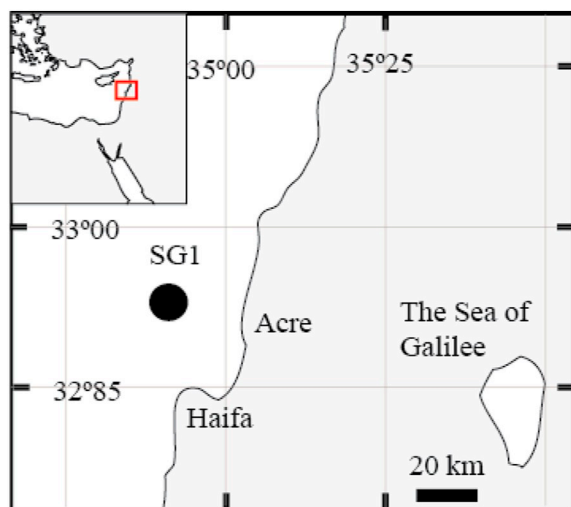


Fig. 1. Study site.

The location of the sampling station sampled in this study (SG1), at the Eastern Mediterranean continental shelf.

extended to 5.5 and 5.75 m, were sampled using a Benthos 2175 piston corer equipped with a plastic liner from sediment. In addition, short sediment cores (0 to 30 cm) were collected with a 0.0625 m² box corer (Ocean Instruments BX 700 AI). The long sediment cores were sliced immediately onboard at intervals of 25–40 cm. The short sediment cores were subsampled with a plastic cylinder with side holes. Directly after slicing, 1.5 mL of sediment was sampled with a cut-off syringe and immediately transferred into 10 mL crimped glass bottles containing 5 mL of 1.5 M NaOH for methane analysis. The glass bottles were flushed with N₂ prior to the cruise, and were constantly flushed with Ar during the sediment sampling. Next, 30 mL aliquots were sampled from the sediment slices using cut-off syringes and were transferred under Ar-flush into 50 mL centrifuge vials. Pore water was separated from these aliquots by centrifuging at 4 °C less than 20 h after sampling. The extracted pore water was filtered through a 0.2 μm PTFE filter (Sigma Aldrich) into the vessels used for each of the analyses. An additional 5 mL sediment aliquot was transferred into a scintillation vial for porosity measurement.

2.2. Pore water chemistry analyses

Dissolved methane concentrations were measured from the headspace of the 10-mL bottles by flame ionization gas-chromatograph with precision (average deviation of the mean of duplicate samples) of ± 0.4 mM. The detection limit of the methane measurement was 50 μmol L⁻¹. The δ¹³C_{CH₄} was measured with a gas source isotope ratio mass-spectrometer equipped with a PreCon interface and a precision of 0.5‰. Pore water for TA analyses was stored in capped plastic syringes at 4 °C until analysis, 2–7 days after the cruise. To verify that the TA of the samples was not changing during their preservation due to the precipitation of carbonate minerals or other processes, we repeatedly measured the TA of one pore water sample over a period of 18 months. These repeated measurements showed no significant changes in TA with time (SI, Table 1). TA measurements were conducted by potentiometric titration (785 Titrino DMP titrator, Metrohm). The titrant (HCl, 0.01 M) was prepared from a commercial standard titrant (Merck). The TA was determined from the titrant volume at the titration end-point. The precision of the TA measurements (average deviation from the mean of duplicate measurements) averaged ± 0.01 mM for the entire dataset. Filtered pore water for DIC and the isotopic composition of DIC (δ¹³C_{DIC}) was stored similarly to the TA samples until analysis 2–3 days after sampling. Approximately 0.3 mL of pore water was injected into a He-flushed vial, containing H₃PO₄. The

¹³C/¹²C ratios of the DIC (expressed as δ¹³C_{DIC} = (R_{sample}/R_{STD} - 1) × 1000, where R_{sample} and R_{STD} denote the ¹³C/¹²C in the sample and in VPDB standard, respectively), were analyzed on a DeltaV Advantage Thermo isotope-ratio mass-spectrometer. The errors on δ¹³C_{DIC} values and DIC values (average deviation from the mean of duplicate measurements) were smaller than 0.1‰ and 0.2 mM, respectively.

Samples for sulfate, magnesium and calcium were sealed in a 1.5 mL snap cap vial and kept at 4 °C until analysis, which was conducted by a Perkin Almer Optima 3300 inductively coupled plasma atomic emission spectrometer using Sc as an internal standard. The analytical error associated with these measurements (average deviations from repeated measurements of a seawater standard) was ± 1%. The detection limit was 0.5 mM for sulfate, 0.5 mM for magnesium and 0.2 mM for calcium.

Samples for sulfide analysis were preserved in the centrifuged pore water by addition of a 20% (wt/v) Zn-acetate solution. Sulfide was measured using the spectroscopic method of Cline (1969) at a wavelength of 665 nm. It should be noted that for the dataset discussed in this article, no measurement exceeded the method detection limit (2 μM).

2.3. Sediment analyses

Sediments for solid phase analyses were prepared by centrifugation, after which excess pore water was decanted from the vials. For organic carbon measurement, carbonate weight percentage and isotopic composition, approximately 10 g of wet sediment was dried at 60 °C until no significant weight change was observed, usually after 60 h. The dry sediments were then ground using a manual mortar grinder to ensure homogeneity of the sediment. More information about these measurements is found in the supplementary information linked to this paper (SI sections 3–7). The sediment porosity was measured by drying approximately 5 g of sediment at 60 °C, until no further weight loss was observed, approximately 48 h later. Porosity was calculated as the weight loss (i.e. water content) from the initial sediment weight.

The reactive iron and pyrite fractions in the sediment were measured after sequential extraction using HCl and HNO₃, respectively (Huerta-Diaz and Morse, 1990). Briefly, a weighed amount of sediment (sediments for sequential Fe-extractions were neither dried nor ground) was placed in 50 mL centrifuge vial. To extract the HCl-soluble iron phases, the sediments were immersed in 10 M HCl and shaken (60 RPM) for 36 h at room temperature. Then, the vials were centrifuged and the acid was decanted into an additional vial. The remaining sediment was then washed three times with double distilled water (DDW), and the washes were decanted into the vial containing the acid after centrifugation. A small volume of the acidic solution was transferred into a 15 mL vial containing 0.1 mL of ascorbic acid (10 mM) and 0.1 mL of Ferrozine reagent dissolved in NH₄-acetate buffer (Stookey, 1970). The Fe(II) concentration in the HCl + DDW mixture was measured spectrophotometrically, using a Spectroquant® Pharo100 spectrophotometer (Merck KGaA, Darmstadt, Germany) at 562 nm. Next, 1 M HNO₃ was added to the sediments, and the same procedure was repeated. In this extraction, the Fe(II) in the acid + DDW mixture resulted from dissolution of pyrite.

2.4. Fluxes and reaction rate calculations

Diffusive fluxes were calculated according to Fick's First Law:

$$F_x = -\phi D_x \frac{\partial C_x}{\partial z} \quad (5)$$

where F_x is the flux of species X (mol cm⁻² d⁻¹), ϕ is the sediment porosity, D_x is the tortuosity corrected diffusion coefficient of species X (corrected according to Boudreau (1997), $D_x = \frac{D_0}{(1 - \ln(\phi^2))}$, cm² d⁻¹), and $\frac{\partial C_x}{\partial z}$ is the vertical concentration gradient of species X (mol cm⁻³). The

values of D_0 were taken from Schulz (2006) for 15 °C.

Reaction rates were calculated according to the diagenetic equation of Berner (1980). Since the processes studied in this work occur at greater depths than those that are affected by bioturbation and irrigation (Treude et al., 2008), and considering the conservative behavior of Na^+ and Cl^- along the sediment column (data not shown) and the small changes in porosity we observed near the SMTZ, which is the focus of this research, we neglect bioturbation and advection, and omit their respective terms from the Berner (1980) equation. Assuming steady-state results in Eq. (6):

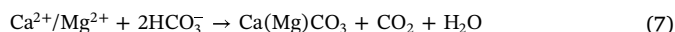
$$\sum R_x = -\frac{1}{\phi} \frac{\partial(\phi D_x \frac{\partial C_x}{\partial z})}{\partial z} \quad (6)$$

The reaction rates were calculated using data smoothed by a MATLAB© smoothing spline algorithm. The tolerance coefficients for the smoothing spline (λ) were 1.7×10^{-5} for the data from September 2015 and 2.7×10^{-5} for the data from January 2017. These values were assigned to produce a realistic, yet smooth trend, constrained by extrapolation to reasonable values at the sediment-seawater interface.

2.5. Model estimations of S-AOM and OSR based on DIC and TA

2.5.1. General approach

The approach applied here for estimating OSR and S-AOM rates is based on the different impact of each of these processes on the DIC and TA in the pore water (Eqs. (1) and (2)). Assuming Eq. (1) stoichiometry, OSR increases both DIC and TA by 2 mol per mole sulfate reduced, hence $\frac{\partial \text{DIC} - \text{OSR}}{\partial \text{SO}_4} = \frac{\partial \text{TA} - \text{OSR}}{\partial \text{SO}_4} = -2$. S-AOM, also increases TA by 2 (Eq. (2)), however, the DIC increase is half, so that $\frac{\partial \text{TA} - \text{S} - \text{AOM}}{\partial \text{SO}_4} = -2$, but $\frac{\partial \text{DIC} - \text{S} - \text{AOM}}{\partial \text{SO}_4} = -1$. The precipitation of carbonate minerals, CaCO_3 , MgCO_3 or $\text{CaMg}(\text{CO}_3)_2$ follows Reactions (7) and (8):



If both calcium and magnesium uptake is due to the precipitation processes described in Eqs. (7) and (8), DIC would decrease by 1, and TA by 2 per mole calcium or magnesium, so that $\frac{\partial \text{DIC}}{\partial \text{Ca}} = \frac{\partial \text{DIC}}{\partial \text{Mg}} = 1$, and $\frac{\partial \text{TA}}{\partial \text{Ca}} = \frac{\partial \text{TA}}{\partial \text{Mg}} = 2$. As all carbonate phases have an identical effect on DIC and TA, we will refer to them as $\text{Ca}(\text{Mg})\text{CO}_3$ hereafter. Methanogenesis by CO_2 reduction, which is the dominant methanogenesis pathway in marine sediments (Whiticar, 1999), follows Reaction (3) and (4). These reactions result in net production of one mol of CO_2 per one mol of CH_4 , so that $\frac{\partial \text{DIC}}{\partial \text{CH}_4} = 1$, and $\frac{\partial \text{TA}}{\partial \text{CH}_4} = 0$. Methanogenesis by acetate fermentation ($\text{CH}_3\text{COOH} \rightarrow \text{CH}_4 + \text{CO}_2$) would have an identical effect on DIC and TA.

Provided that OSR, S-AOM, $\text{Ca}(\text{Mg})\text{CO}_3$ precipitation and methanogenesis are the dominant reactions affecting DIC and TA along a certain depth of the sediment column, the shapes of their respective profiles should reflect their net reaction rate. Therefore, the net reaction rate of TA, at a given depth (z) can be expressed as:

$$\left(\frac{\partial \text{TA}}{\partial t}\right)_z = -2\left(\frac{\partial \text{SO}_4^{2-} - \text{OSR}}{\partial t}\right)_z - 2\left(\frac{\partial \text{SO}_4^{2-} - \text{S} - \text{AOM}}{\partial t}\right)_z + 2\left(\frac{\partial \text{Ca}^{2+}}{\partial t}\right)_z + 2\left(\frac{\partial \text{Mg}^{2+}}{\partial t}\right)_z \quad (9)$$

Similarly, the net reaction rate of DIC, $\left(\frac{\partial \text{DIC}}{\partial t}\right)_z$ at a specific depth can be described as:

$$\left(\frac{\partial \text{DIC}}{\partial t}\right)_z = -2\left(\frac{\partial \text{SO}_4^{2-} - \text{OSR}}{\partial t}\right)_z - \left(\frac{\partial \text{SO}_4^{2-} - \text{S} - \text{AOM}}{\partial t}\right)_z + \left(\frac{\partial \text{Ca}^{2+}}{\partial t}\right)_z + \left(\frac{\partial \text{Mg}^{2+}}{\partial t}\right)_z + \left(\frac{\partial \text{CH}_4}{\partial t}\right)_z \quad (10)$$

The terms $\left(\frac{\partial \text{Ca}^{2+}}{\partial t}\right)_z$, $\left(\frac{\partial \text{Mg}^{2+}}{\partial t}\right)_z$, $\left(\frac{\partial \text{CH}_4}{\partial t}\right)_z$, $\left(\frac{\partial \text{TA}}{\partial t}\right)_z$ and $\left(\frac{\partial \text{DIC}}{\partial t}\right)_z$ were estimated using Eq. (6), from smoothed pore water profiles of calcium, magnesium, methane, TA and DIC, respectively, leaving $\left(\frac{\partial \text{SO}_4^{2-} - \text{OSR}}{\partial t}\right)_z$ and $\left(\frac{\partial \text{SO}_4^{2-} - \text{S} - \text{AOM}}{\partial t}\right)_z$, as unknowns, which were calculated for each depth using Eqs. (9) and (10). Because S-AOM would also affect the methane profile, the term $\left(\frac{\partial \text{CH}_4}{\partial t}\right)_z$ was only used for positive values (= net production of methane), and was nullified in the regions where it showed negative values, which occurred only within the SMTZ. The term $\left(\frac{\partial \text{CH}_4}{\partial t}\right)_z$ represents net methane production, rather than gross methane production. We discuss the sensitivity of the calculated sulfate reduction rates to this approximation later in the text and in the SI.

Notably, there are two underlying assumptions to this approach. The first is that the effect of reactions other than S-AOM, OSR, methanogenesis and carbonate mineral precipitation on TA and DIC in the pore water is negligible, and the second is that the variations in the calcium and magnesium profiles result solely from carbonate mineral precipitation. We discuss these assumptions and test the validity of our results later in the text, as well as in the SI.

3. Field results

3.1. Pore water chemistry

Sulfate concentrations decreased with depth from bottom water values typical for the Southeastern Mediterranean continental shelf (approximately 30mM) to concentrations lower than the detection limit (0.5 mM) below 200 cm below the seafloor in pore water profiles from both cruises. Methane concentrations increased with sediment depth to a maximum of approximately 2–2.5 mM (approximately 25% of saturation levels (Duan and Mao, 2006)) at 300 cm (Fig. 2). Based upon our definition (opposing gradients of pore water sulfate and methane), the SMTZ was located between 100 and 270 cm in September 2015 and between 80 and 210 cm in January 2017.

The DIC concentrations increased from 6 mM at 15 cm to 24 mM in the SMTZ in September 2015, and from 3 mM at 4 cm to 28 mM at 95 cm in January 2017 (Fig. 2). The DIC maxima were accompanied by $\delta^{13}\text{C}_{\text{DIC}}$ minima of -26.5‰ and -25.8‰ . The TA profiles resembled those of DIC, increasing from approximately 6 mM near the seafloor to a maximum 26 mM at the SMTZ in September 2015, and from 4 to 27 mM in January 2017. Below the SMTZ, both DIC and TA decreased to approximately 10 mM, whereas $\delta^{13}\text{C}_{\text{DIC}}$ increased to -15‰ (Fig. 2). These variations may result from methanogenesis, which is also indicated by the isotopic composition of the methane ($\delta^{13}\text{C}_{\text{CH}_4}$, SI Fig. 1) and possibly by other processes, including sulfide oxidation. Processes below the SMTZ are beyond the scope of this work and will not be discussed further.

The concentrations of calcium decreased with depth, from 12 mM at the bottom water to 5 mM at approximately 180 cm, and magnesium decreased from approximately 60 mM to 46mM over the same depth range. On both cruises, a slope break (maximum in the second derivative with depth) in both calcium and magnesium profiles was located in the SMTZ.

A previous study in SG1 (Sela-Adler et al., 2015) showed similar trends in sulfate, methane DIC and $\delta^{13}\text{C}_{\text{DIC}}$. The depth of SMTZ observed by Sela-Adler et al. (2015), however, was approximately 0–50 cm, suggesting high spatial heterogeneity of the geochemical properties of the pore water, as also evident from the differences between our results from September 2015 and January 2017. Studies at a

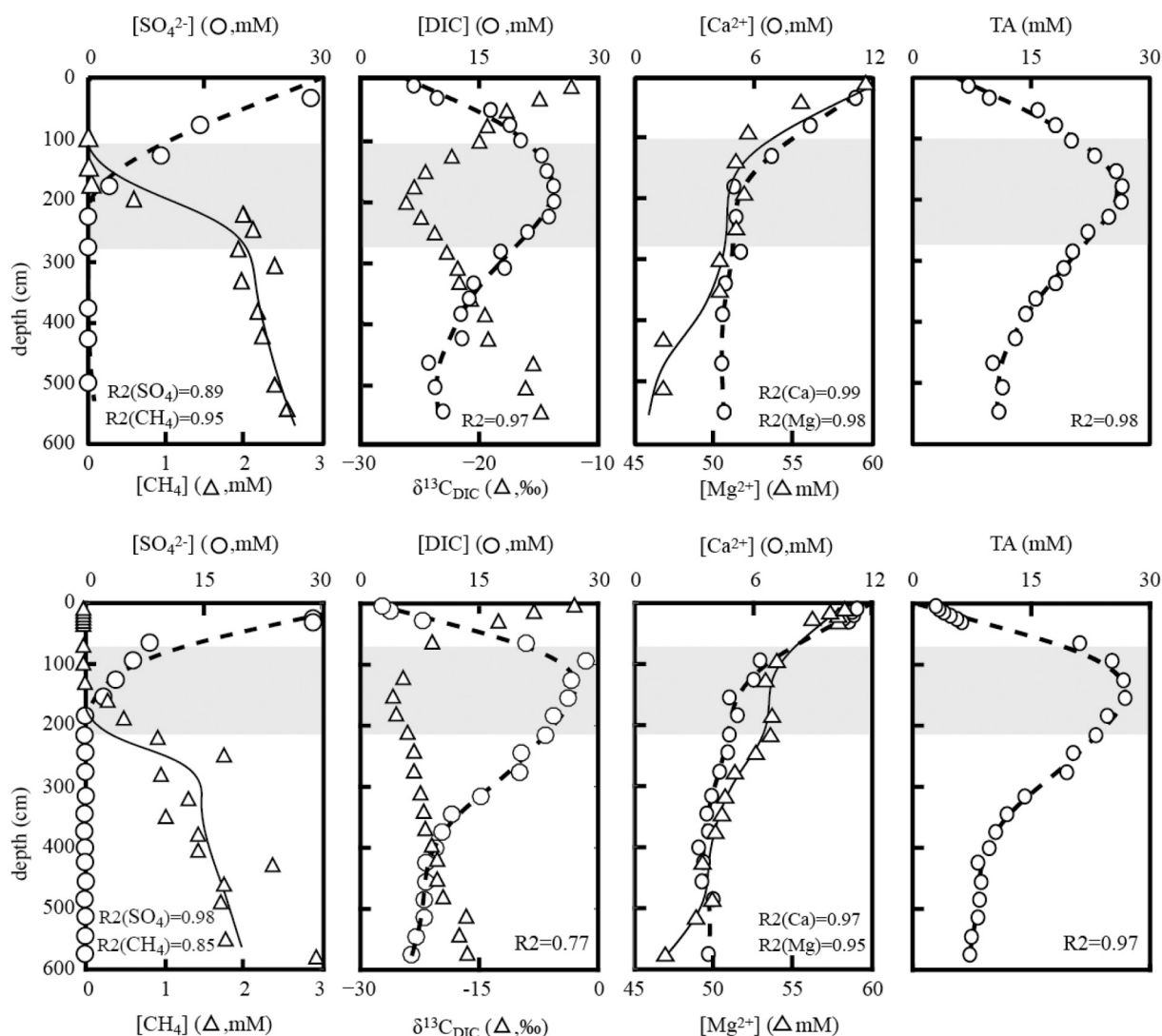


Fig. 2. Pore water chemistry profiles from the Eastern Mediterranean continental shelf, as sampled in September 2015 (upper row) and January 2017 (lower row). The grey zone represent the SMTZ region, defined here as the depth range in which methane and sulfate showed opposite vertical gradients. Notably, this depth range also corresponds to the depth range in which measurable methane and sulfate are found, as well as to the TA, DIC maxima and $\delta^{13}\text{C}_{\text{DIC}}$ minima. The lines represent the smoothed data used for reaction rate calculations (dashed for sulfate, DIC, TA and Ca, solid for methane and magnesium).

site approximately 90 km south of SG1 (Antler et al., 2015; Sela-Adler et al., 2015) showed deeper SMTZ at approximately 600 cm.

3.2. Solid-phase geochemistry

The sediment at station SG1 consists mainly of clays (illite and montmorillite) and albite, which constitute 50–70% of its weight (sediment composition was determined by X-ray diffraction, SI Fig. 2). Quartz is also a significant constituent, composing 15%–25% of the sediment. The porosity (SI Fig. 3) decreased from approximately 0.5 at the sediment surface to 0.45 at 500 cm. The organic carbon content was < 1 wt% throughout the cored sediment column (SI Fig. 4).

The carbonate mineral content (dry wt%) in SG1 varied between 4 and 6% (SI Fig. 5). The isotopic composition of CaCO_3 ($\delta^{13}\text{C}_{\text{CaCO}_3}$) showed an overall decrease of approximately 2.5‰ with depth. A shallow decrease of roughly 1‰ was observed above and within the SMTZ, and a further decrease of 0.8‰ at 350 cm (SI Fig. 6).

HCl-extractable iron (e.g. FeS, reactive iron oxides) showed a notable peak at center of the SMTZ, reaching 6–7 wt% at 150–200 cm (Fig. 3). The concentrations rapidly declined at the bottom of the SMTZ, reaching 1 wt% at 300 cm. HNO_3 -extractable iron (expected to consist

mostly of pyrite; Huerta-Diaz and Morse, 1990) showed two maxima, one at the center of the SMTZ, reaching almost 1 wt%, and another below the SMTZ, at 300–350 cm, reaching almost 2 wt%. The background levels, above the SMTZ and below 350 cm were approximately 0.5 wt%.

4. Calculated S-AOM and OSR rates

In both September 2015 and January 2017, clear peaks of OSR and S-AOM rates were observed. OSR rates peaked at 70 and 100 cm, and S-AOM at 150–160 cm, in September 2015 and January 2017, respectively (Fig. 4). In September 2015, both OSR and S-AOM reached approximately $0.3 \pm 0.2 \text{ nmol cm}^{-3} \text{ d}^{-1}$ at their respective peaks; however, S-AOM declined to zero at 220 cm, whereas OSR maintained positive rates within and below the S-AOM zone, reaching zero only at 270 cm. In January 2017, the calculated OSR rate was higher than it was in September 2015, peaking at $0.7 \pm 0.2 \text{ nmol cm}^{-3} \text{ d}^{-1}$, whereas S-AOM was $0.2 \pm 0.1 \text{ nmol cm}^{-3} \text{ d}^{-1}$. Negative S-AOM rates, as well as deep OSR and S-AOM peaks below the SMTZ were calculated. We attribute these values to processes other than OSR, S-AOM and Ca (Mg) CO_3 precipitation, which also affect DIC and TA, but were not

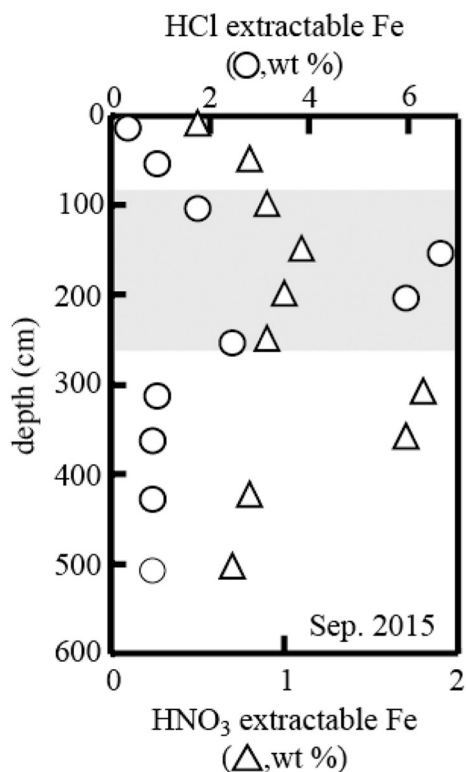


Fig. 3. Solid Fe-phases in SG1 extracted by HCl (FeS, reactive iron oxides) and HNO₃ (predominantly pyrite) Fe-phases in SG1. The grey zone represents the SMTZ.

accounted for by the assumptions underlying our method of calculation (e.g. sulfide oxidation, and/or Fe(III) reduction). Therefore, throughout the remainder of the text, we conservatively assume that our calculations are valid only within the SMTZ. Note that the errors mentioned above and throughout the rest of the text (30% for OSR rates, and 50% for S-AOM rates) are based on sensitivity tests and error analyses, which are described in detail in the SI, section 9.

In September 2015, the net sulfate flux into the SMTZ induced by OSR was $12 \pm 4 \text{ nmol cm}^{-2} \text{ d}^{-1}$ (Table 1, calculated by integrating the OSR rates between 100 and 270 cm), and the flux induced by S-AOM was $20 \pm 10 \text{ nmol cm}^{-2} \text{ d}^{-1}$. In January 2017, the SMTZ

Table 1
Mass balance calculations in the sediment column.

	September 2015	January 2017
a. SMTZ depth range used in calculations (cm bsfl)		
	100–270	80–210
b. Integrated sulfate reduction rates ($\text{nmol cm}^{-2} \text{ d}^{-1}$)		
OSR	12 ± 4	34 ± 8
S-AOM	20 ± 10	20 ± 10
c. Fluxes into/out of the SMTZ ($\text{nmol cm}^{-2} \text{ d}^{-1}$)		
F_{Ca}	-8 ± 4	-10 ± 5
F_{Mg}	-9 ± 4	-5 ± 2
F_{CH_4}	8 ± 4	3 ± 2
$F_{\text{DIC, TOP}}$	30 ± 7	72 ± 17
$F_{\text{DIC, BOTTOM}}$	-18 ± 4	-27 ± 6
$F_{\text{DIC, IN}}$	44 ± 15	87 ± 22
$F_{\text{DIC, OUT}}$	35 ± 10	84 ± 20
d. $\delta^{13}\text{C}_{\text{DIC}}$ in the SMTZ		
δ_{OSR}	-20%	
$\delta_{\text{S-AOM}}$	-76%	-85%
δ_{TOP}	-31%	-30%
δ_{BOTTOM}	-30%	-25%
$\delta_{\text{DIC, IN}}$	-46%	-35%
$\delta_{\text{DIC, OUT}}$	-44%	-34%
e. Fractions of sulfate reduction and DIC contribution by OSR and S-AOM		
$f_{\text{SO}_4, \text{OSR}}$	0.4	0.6
$f_{\text{DIC, OSR}}$	0.5	0.8
$f_{\text{SO}_4, \text{S-AOM}}$	0.6	0.4
$f_{\text{DIC, S-AOM}}$	0.5	0.2

integrated (80–210 cm) sulfate reduction rate by OSR and S-AOM were 34 ± 8 and $20 \pm 10 \text{ nmol cm}^{-2} \text{ d}^{-1}$, respectively.

4.1. Sulfate reduction rates calculated from pore water sulfate profiles

To validate the underlying assumptions of our calculations and to test the accuracy of our calculated OSR and S-AOM rates (Fig. 4), we first compare these rates to the corresponding sulfate consumption rates calculated from the pore water concentration profile (Fig. 2). Since the calculated OSR and S-AOM were expressed as net sulfate uptake rates, the sum of these two reactions at a given depth (z) should be equal to the net consumption of sulfate at the same depth:

$$\left(\frac{\partial \text{SO}_4^{2-}}{\partial t}\right)_z = \left(\frac{\partial \text{SO}_4^{2-}}{\partial t} - \text{OSR}\right)_z + \left(\frac{\partial \text{SO}_4^{2-}}{\partial t} - \text{S-AOM}\right)_z \quad (11)$$

where $\left(\frac{\partial \text{SO}_4^{2-}}{\partial t}\right)_z$ is calculated according to Eq. (6), using the sulfate data

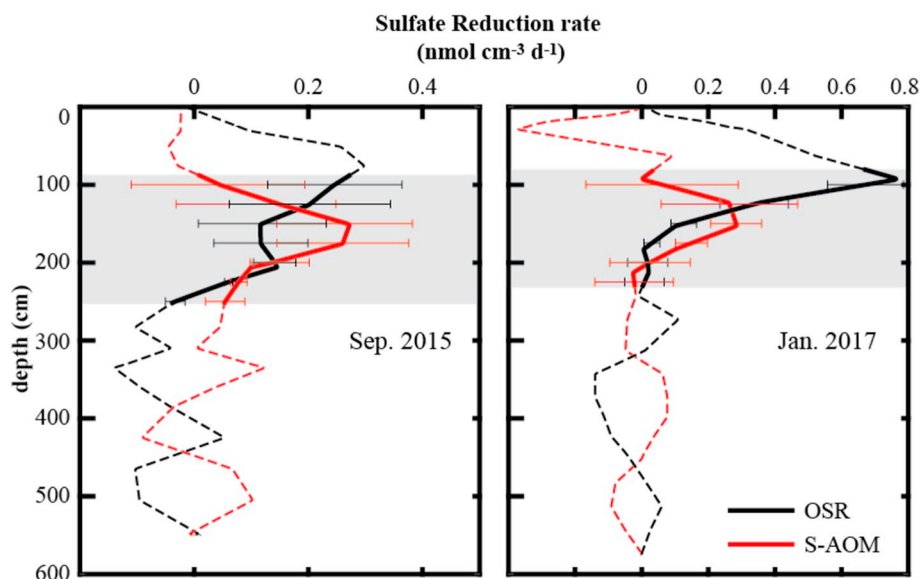
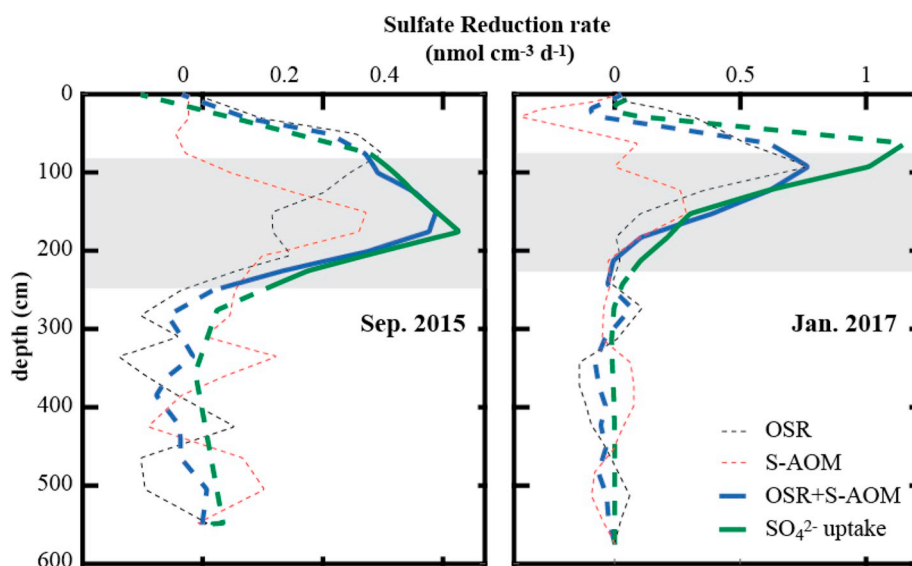


Fig. 4. Rates of sulfate reduction by oxidation of organic material (OSR, black line) and by anaerobic oxidation of methane (S-AOM, red line), as calculated from the DIC, TA calcium, magnesium and methane data. In both datasets, OSR peaked above S-AOM. The S-AOM peaks coincided with the sulfate and methane gradients, as well as with the DIC and TA maxima and the $\delta^{13}\text{C}_{\text{DIC}}$ minimum (Fig. 2). The error bars are shown for every 20th data point and reflect mainly the uncertainty associated with the magnesium uptake mechanism and the rate of methanogenesis (see supplementary information section 9 for error estimation). The grey area represents the SMTZ, in which opposing gradients of sulfate and methane were present. The dashed lines above and below the SMTZ indicate that the model assumptions used for S-AOM and OSR calculations are not valid in these depths of the sediment column. (For interpretation of the references to colour in this figure legend, the reader is referred to the web version of this article.)



(Fig. 2). When the sum of the obtained S-AOM and OSR rate profiles is compared to the profile of $\left(\frac{\partial \text{SO}_4^{2-}}{\partial t}\right)$ (Fig. 5), the two profiles are in good agreement within the SMTZ, for the September 2015 data. In January 2017, the general trends agree, however, the OSR + S-AOM are smaller than $\left(\frac{\partial \text{SO}_4^{2-}}{\partial t}\right)$. We attribute this disagreement to the sampling resolution, which may have not captured the full extent of the OSR peak at approximately 100 cm. The high DIC concentration at this depth (Fig. 2), which exceeds the smoothed line used for the calculation corroborates this explanation. Notably, these profiles are independent of each other, because $\left(\frac{\partial \text{SO}_4^{2-} - \text{OSR}}{\partial t}\right)$ and $\left(\frac{\partial \text{SO}_4^{2-} - \text{S-AOM}}{\partial t}\right)$ were calculated without using the sulfate data.

4.2. Comparison of calculated S-AOM fluxes to the methane flux

The stoichiometry of the S-AOM reaction (Eq. (2)) suggests a 1:1 ratio between the uptake of sulfate and the uptake of methane. Therefore, to compare the calculated S-AOM rates with the diffusive methane flux (F_{CH_4}) into the SMTZ, we compared the depth-integrated S-AOM rates (fluxes) within the SMTZ with the methane fluxes into the SMTZ, as calculated from the methane data (Fig. 2) using Eq. (5). For both September and January, we used the depth interval between the center of the SMTZ and the depth with the highest CH_4 concentration at the SMTZ bottom or immediately below. This selection yielded the largest CH_4 fluxes (F_{CH_4}) into the SMTZ. Nevertheless, the integrated S-AOM rates were still considerably larger. In September 2015, F_{CH_4} equaled $8 \pm 4 \text{ nmol cm}^{-2} \text{ d}^{-1}$ (Table 1) and the integrated S-AOM was $20 \pm 10 \text{ nmol cm}^{-2} \text{ d}^{-1}$. In January 2017, F_{CH_4} was 3 ± 2 , whereas the integrated S-AOM was $20 \pm 10 \text{ nmol cm}^{-2} \text{ d}^{-1}$, respectively. We attribute the lower F_{CH_4} to de-gassing during the sampling, which resulted in diminished methane gradients.

4.3. DIC and DI^{13}C fluxes

To calculate the DIC flux induced by OSR, we integrated the OSR rates along the SMTZ, and multiplied the result by two, according to the reaction stoichiometry (Eq. (1)). In the case of S-AOM, we simply used the integrated rates, since the DIC addition equals the sulfate consumption (Eq. (2)). Therefore, the incoming DIC flux ($F_{\text{DIC,IN}}$) is equal to:

$$F_{\text{DIC,IN}} = - \int_{\text{bottom SMTZ}}^{\text{top SMTZ}} \left(\frac{\partial \text{SO}_4^{2-} - \text{S-AOM}}{\partial t} \right)_z dz - 2 \int_{\text{bottom SMTZ}}^{\text{top SMTZ}} \left(\frac{\partial \text{SO}_4^{2-} - \text{OSR}}{\partial t} \right)_z dz \quad (12)$$

which yields $44 \pm 15 \text{ nmol C cm}^{-2} \text{ d}^{-1}$ in September 2015 and $87 \pm 22 \text{ nmol C cm}^{-2} \text{ d}^{-1}$ in January 2017 (Table 1). $F_{\text{DIC,IN}}$ can be compared to sum of the diffusive fluxes leaving the SMTZ ($F_{\text{DIC,OUT}}$):

$$F_{\text{DIC,OUT}} = F_{\text{DIC}}^{\text{top}} - F_{\text{DIC}}^{\text{bottom}} - F_{\text{Ca}} - F_{\text{Mg}} \quad (13)$$

where $F_{\text{DIC}}^{\text{top}}$ and $F_{\text{DIC}}^{\text{bottom}}$ are the diffusive DIC fluxes at the top and bottom of the SMTZ, respectively, and F_{Ca} and F_{Mg} are the diffusive fluxes of calcium and magnesium into the SMTZ, which were assumed to represent Ca(Mg)CO_3 precipitation. Using Eq. (5) to calculate the diffusive fluxes, we obtain $F_{\text{DIC,OUT}} = 35 \pm 10$ and $84 \pm 20 \text{ nmol C cm}^{-2} \text{ d}^{-1}$ in September 2015 and January 2017 (respectively), which is in good agreement with $F_{\text{DIC,IN}}$ obtained for both cruises (44 ± 15 in September 2015 and 87 ± 22 in January 2017, Table 1). We note that the precipitation of other carbonate minerals, namely siderite (FeCO_3) may constitute an additional sink term to Eq. (13), which might reduce the difference between $F_{\text{DIC,IN}}$ and $F_{\text{DIC,OUT}}$. Specifically, the precipitation of siderite can be estimated using the Poulton and Canfield (2005) protocol for separating the HCl-extractable Fe to its sub-constituents, which was not conducted as part of this study.

To calculate the ^{13}C mass-balance in the SMTZ, we adopt the approach described by Komada et al. (2016). We first calculate the $\delta^{13}\text{C}$ of the DIC flux entering the SMTZ (flux divergence) after Eq. (14):

$$F_{\text{DIC,IN}} \times \delta_{\text{DIC,IN}} = \int_{\text{bottom SMTZ}}^{\text{top SMTZ}} \left(\frac{\partial \text{SO}_4^{2-} - \text{S-AOM}}{\partial t} \right)_z \delta_{\text{S-AOM}} dz + 2 \int_{\text{bottom SMTZ}}^{\text{top SMTZ}} \left(\frac{\partial \text{SO}_4^{2-} - \text{OSR}}{\partial t} \right)_z \delta_{\text{OSR}} dz \quad (14)$$

where δ_{OSR} and $\delta_{\text{S-AOM}}$ represent the $\delta^{13}\text{C}$ values of the DIC flux into the SMTZ, induced by OSR and S-AOM, respectively. We assign δ_{OSR} as -20% , roughly representing $\delta^{13}\text{C}$ of marine organic material (Zeebe and Wolf-Gladrow, 2001), and assume no isotopic fractionation during OSR (Boehme et al., 1996; Govert and Conrad, 2008; Londry and Marais, 2003). $\delta_{\text{S-AOM}}$ is estimated from the slope of the $[\text{CH}_4] \times \delta^{13}\text{C}_{\text{methane}}$ vs. $[\text{CH}_4]$ mixing-net reaction plot (Sayles and Curry, 1988) (Fig. 6). $\delta_{\text{DIC,IN}}$ can be compared with the $\delta^{13}\text{C}_{\text{DIC}}$ of the diffusive fluxes leaving the SMTZ:

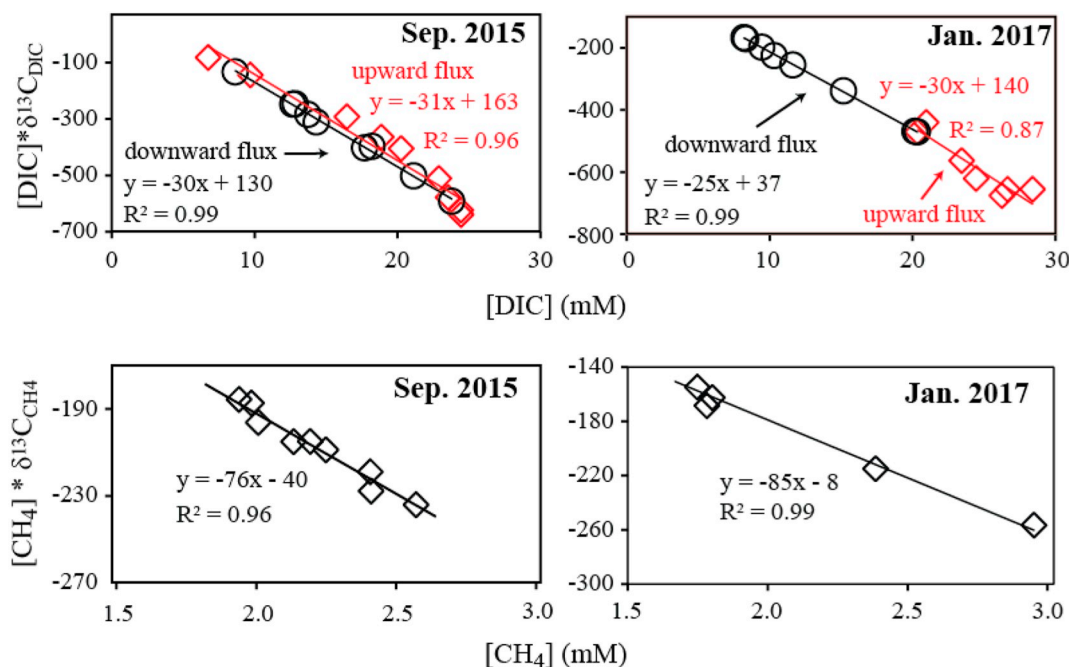


Fig. 6. Mixing/net-reaction plots for DIC and methane in the SMTZ. The y-axis represents the product of the concentration (DIC or methane) and its isotopic composition ($\delta^{13}\text{C}_{\text{DIC}}$ or $\delta^{13}\text{C}_{\text{CH}_4}$). The x-axis is the corresponding concentration. The slope of each plot represents the isotopic $\delta^{13}\text{C}$ value of the carbon entering or leaving the SMTZ (Komada et al., 2016; Sayles, 1979). Note that DIC fluxes from the SMTZ extend both upward (red diamonds) and downward (black circles), with a different slope per each flux. (For interpretation of the references to colour in this figure legend, the reader is referred to the web version of this article.)

$$F_{\text{DIC,OUT}}\delta_{\text{DIC,OUT}} = F_{\text{DIC}}^{\text{top}}\delta_{\text{top}} - F_{\text{DIC}}^{\text{bottom}}\delta_{\text{bottom}} \quad (15)$$

where δ_{top} and δ_{bottom} are the $\delta^{13}\text{C}_{\text{DIC}}$ fluxes at the top and bottom of the SMTZ, respectively, as calculated from the $\text{DIC} \times \delta^{13}\text{C}_{\text{DIC}}$ vs. DIC mixing-net reaction plot of the relevant depths in the sediment (Fig. 6). Eq. (14) yielded $\delta_{\text{DIC,IN}}$ of -46‰ and -35‰ for September 2015 and January 2017, respectively (Table 1). $\delta_{\text{DIC,OUT}}$ agreed with $\delta_{\text{DIC,IN}}$ within 2‰. The variations induced by considering isotopic fractionation (ϵ) during $\text{Ca}(\text{Mg})\text{CO}_3$ precipitation, with $\epsilon = 3\text{‰}$ (Zeebe and Wolf-Gladrow, 2001) were lower than the uncertainties induced by other parameters, therefore we assumed that $\text{Ca}(\text{Mg})\text{CO}_3$ precipitation does not fractionate C isotopes.

5. Discussion

The use of DIC, TA, methane, calcium and magnesium yielded reliable calculations of net sulfate reduction rates. Pore water sulfate profiles (Fig. 2) showed a clear signature of sulfate consumption within the SMTZ. In addition, the decrease in calcium and magnesium concentrations (Fig. 2), the decrease in $\delta^{13}\text{C}_{\text{CaCO}_3}$ (SI Fig. 6) and the high saturation levels for carbonate minerals (SI Fig. 7) indicated that carbonate minerals precipitate from the ^{13}C -depleted DIC pool in the pore water of SG1. The S-AOM and OSR rates (Fig. 4) calculated from TA and DIC peaked within and above the SMTZ (respectively) and agreed with the total sulfate reduction rate calculated independently from the sulfate profiles (Fig. 5). The integrated reaction rates within the SMTZ (i.e. the fluxes) were in good agreement with the bulk fluxes of DIC, and with the ^{13}C fluxes calculated from the DIC and $\delta^{13}\text{C}$ data (Table 1).

5.1. Comparison of fluxes and reaction rates in the Southeastern Mediterranean sediments to other systems

Our calculations show that within the SMTZ, S-AOM and OSR reduce approximately an equal fraction of the sulfur (Table 1). A nearly equal fraction of sulfate reduced by S-AOM and OSR was also estimated for the SMTZ at the Santa Barbara Basin (Berelson et al., 2005; Komada et al., 2016). Furthermore, the maximum OSR ($0.8 \text{ nmol cm}^{-3} \text{ day}^{-1}$)

and S-AOM ($0.3 \text{ nmol cm}^{-3} \text{ day}^{-1}$) rates we calculated (Fig. 4) are similar to the rates calculated from sulfate and methane profiles in sediments from the Black Sea and Limfjorden (Jørgensen and Parkes, 2010; Jørgensen et al., 2001). Although these systems have different characteristics, for example with respect to TOC (range 4–15 wt%), oxygen penetration depth (range 0–6 mm) and sedimentation rate (range $0.2\text{--}4 \text{ cm yr}^{-1}$) (Jørgensen, 1977; Leventhal, 1983; Reimers et al., 1996) and furthermore differ from our study site (TOC = 0.5 wt% (SI Fig. 4), sedimentation rate = 10 mm yr^{-1} (Bareket et al., 2016)), the general agreement between our results and those from the previous studies demonstrates that our method yields reasonable results that fall within previously determined ranges for these processes.

In spite of the fact that the Southeastern Mediterranean basin is an ultra-oligotrophic basin, with relatively high deep water oxygen concentrations (Kress and Herut, 2001), the sulfate reduction rates we calculated in the SMTZ at SG1 resemble rates calculated for anoxic and/or eutrophic regions. The similarity between sulfate reduction rates in the ultra-oligotrophic Southeastern Mediterranean and these eutrophic regions suggests that “external” methane, which is not the product of degradation of organic material originating in the water column but rather derives from deeper deposits, provides an important source of reducing power to the SMTZ. Such deep methane deposits and upward fluxes are common in many continental margins (e.g. (Milkov and Sassen, 2002; Milkov, 2004; Paull et al., 2008; Zhang and Lanoil, 2004)).

5.2. The fate of sulfide in the SMTZ of SG1

Despite ongoing sulfate reduction, no sulfide was detected in the SMTZ or in any other part of the sediment column. Furthermore, sulfate concentrations in the SMTZ decreased below the detection limit. Taken together, this indicates that the net sulfide consumption is equal to sulfate reduction; that is, S-AOM + OSR. The further reaction of sulfide produced from sulfate reduction from either OSR or S-AOM would affect the pore water TA, and therefore Eq. (9) can be generalized to Eq. (16), such that it will account for these reactions,

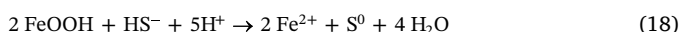
$$\left(\frac{\partial \text{TA}}{\partial t}\right)_z = -\alpha \left(\frac{\partial \text{SO}_4^{2-}}{\partial t} - \text{OSR}\right)_z - \alpha \left(\frac{\partial \text{SO}_4^{2-}}{\partial t} - \text{S} - \text{AOM}\right)_z + 2 \left(\frac{\partial \text{Ca}^{2+}}{\partial t}\right)_z + 2 \left(\frac{\partial \text{Mg}^{2+}}{\partial t}\right)_z \quad (16)$$

where the coefficient α accounts not only for the effects of OSR and S-AOM on TA, but also for the net effect of the following sulfide oxidation processes.

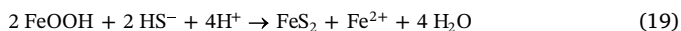
One of the main processes in the sulfur cycle of marine sediments that removes sulfide from pore water is the formation of pyrite (Fike et al., 2015 and references therein). In marine sediments, pyrite formation likely proceeds predominately through the net reaction of zero-valent sulfur (likely as polysulfide) with iron (c.f. Rickard and Luther (2007); Eq. (17)).



This reaction effectively removes 2 units of TA for every unit of pyrite formed. In order for S^0 to be formed, however, sulfide produced via sulfate reduction must first be oxidized. This can occur biologically, or abiotically via reaction with iron oxides (Eq. (18)) (Findlay et al., 2014; Yao and Millero, 1993, 1996),



Sulfide oxidation by this reaction increases TA (+4 units) through the consumption of protons. If Eq. (18) is coupled to pyrite formation, which is likely in most sediments, pyrite formation results in a net increase in TA of 2 stoichiometric units (Eq. (19)).



Another possible pathway for pyrite formation is the reaction of FeS with H_2S ; however, this pathway is not expected to dominate in marine sediments at circum-neutral pH (Rickard and Luther, 2007).

Sulfide can also react with the reduced iron to form FeS via Eq. (20):



which removes two units of alkalinity.

Therefore, returning to Eq. (16), if a mole unit of sulfate is reduced by either OSR or S-AOM and then oxidized by iron-oxide (Eq. (18)), α will equal six. If its reduction by S-AOM or OSR is followed by reaction of iron to form either pyrite or iron sulfide (Eqs. (17) and (20), respectively), α will equal zero. Assuming that all sulfide consumption in the SMTZ is carried by either of these processes, the relations between α and the net reduction and oxidation reactions of sulfur can be described by Eq. (21),

$$\alpha = 2 - 2 \times f_{\text{precip}} + 4 \times (1 - f_{\text{precip}}) \quad (21)$$

where 2 is the stoichiometric coefficient of either OSR or S-AOM on TA, f_{precip} is the fraction of the reduced sulfur which is fixed as either pyrite or FeS, and $(1 - f_{\text{precip}})$ is the fraction of sulfide that is converted to S^0 by reaction with iron-oxide.

Fig. 7 shows the integrated OSR and S-AOM rates in the SMTZ, as a function of f_{precip} . Only when f_{precip} is between 0.5 and 0.7, the integrated rates of both OSR and S-AOM in the SMTZ are positive. Because negative integrated rates of either processes are highly unlikely, we assume that 0.5–0.7 represents the probable values of f_{precip} . This range can also be tested by examining the ^{13}C mass balance. The choice of f_{precip} changes $\delta_{\text{DIC,IN}}$ (Fig. 7), but does not affect $\delta_{\text{DIC,OUT}}$, which depends mainly on the DIC and $\delta^{13}\text{C}_{\text{DIC}}$ profiles. The best agreement between $\delta_{\text{DIC,IN}}$ and $\delta_{\text{DIC,OUT}}$ is obtained at $f_{\text{precip}} = 0.65$. We therefore estimate that of the reduced sulfate, $65 \pm 10\%$ precipitates as FeS and pyrite, both of which are above saturation (SI Fig. 7) while the remaining $35 \pm 10\%$ is oxidized and precipitates as S^0 . Regretfully, we did not break down the HCl-extractable fraction to its sub-constituents (Poulton and Canfield, 2005), and consequently we cannot verify that the HCl-extractable peak in the SMTZ (Fig. 3) is indeed FeS. However, the low rates of pyrite precipitation (SI Fig. 12) and the high degree of

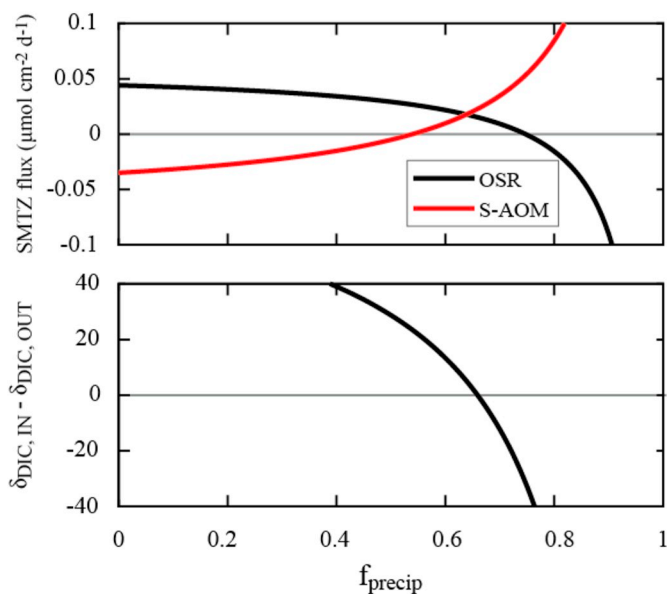


Fig. 7. The effect of the fraction of sulfide that precipitates as pyrite and FeS (f_{precip}) on the sulfate flux into the SMTZ from OSR and S-AOM (top panel), and on the difference between the $\delta^{13}\text{C}$ fluxes in and out of the SMTZ (bottom panel). The calculation was done for the September 2015 dataset. Positive sulfate reduction rates are obtained when $f_{\text{precip}} = 0.65 \pm 0.1$. At this values, the $\delta^{13}\text{C}$ fluxes to the SMTZ are at optimal agreement.

FeS supersaturation (SI Fig. 7) we estimated for the SMTZ, support our suggestion that the majority of the reduced sulfate in the SMTZ eventually precipitates as FeS.

5.3. Total alkalinity as a proxy for sulfate reduction rates

The agreement between the sulfate reduction rates we calculated using TA and DIC (with corrections for Ca^{2+} and Mg^{2+}) and the rates and fluxes calculated from independent proxies (SO_4^{2-} , Fig. 5 and $\delta^{13}\text{C}$, Table 1) demonstrate that TA can be used as a quantitative proxy for sulfate reduction rates, beyond its common use as a diagnostic tool to identify the dominant processes in pore waters. The main advantages of TA as such a proxy are its low sensitivity to gas-exchange during the sampling and the high-quality data (precision of approximately 0.1%) that it yields with relatively common equipment. It should be noted, however, that the decrease in pressure and increase in temperature that the sediment experiences during recovery might lead to an increase in the saturation level for carbonate minerals ($\Omega = [\text{Ca}^{2+}][\text{CO}_3^{2-}]/K_{\text{SP}}$, where K_{SP} is the stoichiometric solubility product for either calcite or aragonite), and consequently, to a decrease in TA due to precipitation (e.g. (Sauvage et al., 2014; Sayles and Manheim, 1975)). This process, however, has little effect in pore water from shallow to intermediate depths. For example, Ω values for calcite and aragonite in the pore water from SG1 (SI Fig. 7) experience an increase of < 5% during their extraction from a depth of 80 m and temperature of 16 °C to surface at 20 °C (this calculation was conducted with a modified version of the CO2sys program, which accounts for $\text{Si}(\text{OH})_4$, soluble reactive phosphate as well as for NH_3 (SI Fig. 10) and H_2S (Pierrot et al., 2006; Xu et al., 2017)). In light of these advantages and the results we presented here, we suggest that TA profiles, along with DIC, Ca^{2+} , Mg^{2+} and CH_4 can be used in future studies to estimate net sulfate reduction rates.

6. Conclusions

In this study, we propose that TA can be applied to disentangle and quantify sulfate reduction rates in marine sediments. We demonstrate such an application in the Mediterranean continental shelf, where,

using calculations based upon the different effects that OSR and S-AOM have on TA and DIC concentrations, we calculated that an equal fraction of sulfate is reduced by both pathways within the SMTZ. These calculated S-AOM and OSR rates are similar to rates reported in other studies based on sulfate fluxes. As sulfide was not detected in the pore water, despite sulfate reduction, TA and DIC profiles are likely affected by the further reaction of sulfide produced during sulfate reduction either through oxidation or pyrite formation. We roughly estimate that the majority of the sulfide produced by sulfate reduction precipitates as iron sulfide minerals. In light of our results, and the analytical advantages of TA, we suggest that TA profiles can be used to estimate of sulfate reduction rates in marine sediments.

Acknowledgments

The authors thank the captain and crew of the R/V *Bat Galim* and R/V *Shikmona* from the Israel Oceanographic and Limnological Research for their assistance during field sampling. We are thankful to E. Eliani-Russak for technical help in the lab, and to Shimon Feinstein, L. Freitas and E. Danon for their help in measuring TOC. We thank Boaz Lazar for his help through many fruitful discussions. This research was supported by Grants 212-17-024 and 214-17-011 from the Israel Ministry of National Infrastructure, Energy and Water (to O. Sivan and B. Herut) and by the Israel Science Foundation (#643/12). E. Wurgaft's activities were also supported by a scholarship from The Kreitman School of Advanced Graduate Studies. A. J. Findlay acknowledges support from a Fulbright postdoctoral fellowship and a Marie Curie European Fellowship (SedSulphOx, MSCA 746872).

Appendix A. Supplementary data

Supplementary data to this article can be found online at <https://doi.org/10.1016/j.marchem.2019.03.004>.

References

- Aharon, P., Fu, B.S., 2000. Microbial sulfate reduction rates and sulfur and oxygen isotope fractionations at oil and gas seeps in Deepwater Gulf of Mexico. *Geochim. Cosmochim. Acta* 64 (2), 233–246.
- Aller, R.C., Rude, P.D., 1988. Complete oxidation of solid-phase sulfides by manganese and bacteria in anoxic marine-sediments. *Geochim. Cosmochim. Acta* 52 (3), 751–765.
- Aller, R.C., Mackin, J.E., Cox, R.T., 1986. Diagenesis of Fe and S in Amazon inner shelf muds - apparent dominance of Fe reduction an implications for the genesis of ironstones. *Cont. Shelf Res.* 6 (1–2), 263–289.
- Antler, G., et al., 2014. Sulfur and oxygen isotope tracing of sulfate driven anaerobic methane oxidation in estuarine sediments. *Estuar. Coast. Shelf Sci.* 142, 4–11.
- Antler, G., Turchyn, A.V., Herut, B., Sivan, O., 2015. A unique isotopic fingerprint of sulfate-driven anaerobic oxidation of methane. *Geology* 43 (7), 619–622.
- Arndt, S., et al., 2013. Quantifying the degradation of organic matter in marine sediments: a review and synthesis. *Earth Sci. Rev.* 123, 53–86.
- Bareket, M.M., Bookman, R., Katsman, R., de Stigter, H., Herut, B., 2016. The role of transport processes of particulate mercury in modifying marine anthropogenic secondary sources, the case of Haifa bay, Israel. *Mar. Pollut. Bull.* 105 (1), 286–291.
- Barnes, R.O., Goldberg, E.D., 1976. Methane production and consumption in anoxic marine-sediments. *Geology* 4 (5), 297–300.
- Berelson, W.M., et al., 2005. Anaerobic diagenesis of silica and carbon in continental margin sediments: discrete zones of CO₂ production. *Geochim. Cosmochim. Acta* 69 (19), 4611–4629.
- Berner, R.A., 1980. *Early Diagenesis: A Theoretical Approach*. Princeton University Press.
- Berner, R.A., 1982. Burial of organic carbon and pyrite sulfur in the modern ocean: its geochemical and environmental significance. *Am. J. Sci.* (United States) 282.
- Berner, R.A., Scott, M.R., Thomlinson, C., 1970. Carbonate alkalinity in pore waters of anoxic marine sediments. *Limnol. Oceanogr.* 15 (4), 544–549.
- Blair, N.E., Aller, R.C., 1995. Anaerobic methane oxidation on the Amazon shelf. *Geochim. Cosmochim. Acta* 59 (18), 3707–3715.
- Boehme, S., Blair, N., Chanton, J., Martens, C., 1996. A mass balance of C-13 and C-12 in an organic-rich methane-producing marine sediment. *Geochim. Cosmochim. Acta* 60 (20), 3835–3848.
- Borowski, W.S., Paull, C.K., Ussler, W., 1996. Marine pore-water sulfate profiles indicate in situ methane flux from underlying gas hydrate. *Geology* 24 (7), 655–658.
- Borowski, W.S., Hoehler, T.M., Alperin, M.J., Rodriguez, N.M., Paull, C.K., 2000. Significance of Anaerobic Methane Oxidation in Methane-Rich Sediments Overlying the Blake Ridge Gas Hydrates, Proceedings of the Ocean Drilling Program, Scientific Results. pp. 87–99.
- Boudreau, B.P., 1997. *Diagenetic Models and their Implementation*, 505. Springer Berlin.
- Burdige, D.J., Komada, T., 2011. Anaerobic oxidation of methane and the stoichiometry of remineralization processes in continental margin sediments. *Limnol. Oceanogr.* 56 (5), 1781–1796.
- Cline, J.D., 1969. Spectrophotometric determination of hydrogen sulfide in natural waters 1. *Limnol. Oceanogr.* 14 (3), 454–458 May.
- Duan, Z.H., Mao, S.D., 2006. A thermodynamic model for calculating methane solubility, density and gas phase composition of methane-bearing aqueous fluids from 273 to 523 K and from 1 to 2000 bar. *Geochim. Cosmochim. Acta* 70 (13), 3369–3386.
- Egger, M., et al., 2016. Anaerobic oxidation of methane alters sediment records of sulfur, iron and phosphorus in the Black Sea. *Biogeosciences* 13 (18), 5333.
- Emerson, S., et al., 1980. Early diagenesis in sediments from the eastern equatorial Pacific. 1. Pore water nutrient and carbonate results. *Earth Planet. Sci. Lett.* 49 (1), 57–80.
- Fike, D.A., Bradley, A.S., Rose, C.V., 2015. Rethinking the ancient sulfur cycle. *Annu. Rev. Earth Planet. Sci.* 43 (43), 593–622.
- Findlay, A.J., et al., 2014. Distribution and size fractionation of elemental sulfur in aqueous environments: the Chesapeake Bay and mid-Atlantic ridge. *Geochim. Cosmochim. Acta* 142, 334–348.
- Fossing, H., Jørgensen, B.B., 1989. Measurement of bacterial sulfate reduction in sediments: evaluation of a single-step chromium reduction method. *Biogeochemistry* 8 (3), 205–222.
- Fossing, H., Ferdelman, T.G., Berg, P., 2000. Sulfate reduction and methane oxidation in continental margin sediments influenced by irrigation (South-East Atlantic off Namibia). *Geochim. Cosmochim. Acta* 64 (5), 897–910.
- Froelich, P.N., et al., 1979. Early oxidation of organic-matter in pelagic sediments of the eastern equatorial Atlantic - suboxic diagenesis. *Geochim. Cosmochim. Acta* 43 (7), 1075–1090.
- Gieskes, J., et al., 2005. A study of the chemistry of pore fluids and authigenic carbonates in methane seep environments: Kodiak trench, hydrate ridge, Monterey Bay, and Eel River basin. *Chem. Geol.* 220 (3–4), 329–345.
- Govert, D., Conrad, R., 2008. Carbon isotope fractionation by sulfate-reducing Bacteria using different pathways for the oxidation of acetate. *Environ. Sci. Technol.* 42 (21), 7813–7817.
- Holmkvist, L., Ferdelman, T.G., Jørgensen, B.B., 2011. A cryptic sulfur cycle driven by iron in the methane zone of marine sediment (Aarhus Bay, Denmark). *Geochim. Cosmochim. Acta* 75 (12), 3581–3599.
- Hsu, T.W., Jiang, W.T., Wang, Y.S., 2014. Authigenesis of vivianite as influenced by methane-induced sulfidization in cold-seep sediments off southwestern Taiwan. *J. Asian Earth Sci.* 89, 88–97.
- Huerta-Diaz, M.A., Morse, J.W., 1990. A quantitative method for determination of trace-metal concentrations in sedimentary pyrite. *Mar. Chem.* 29 (2–3), 119–144.
- Iversen, N., Jørgensen, B., 1985. Anaerobic methane oxidation rates at the sulfate-methane transition in marine sediments from Kattegat and Skagerrak (Denmark). *Limnol. Oceanogr.* 30 (5), 944–955.
- Jørgensen, B.B., 1977. Sulfur cycle of a coastal marine sediment (Limfjorden, Denmark). *Limnol. Oceanogr.* 22 (5), 814–832.
- Jørgensen, B.B., 1982. Mineralization of organic-matter in the sea bed - the role of sulfate reduction. *Nature* 296 (5858), 643–645.
- Jørgensen, N.O., 1992. Methane-derived carbonate cementation of marine sediments from the Kattegat, Denmark: geochemical and geological evidence. *Mar. Geol.* 103 (1–3), 1–13.
- Jørgensen, B.B., Kasten, S., 2006. Sulfur cycling and methane oxidation. In: *Marine Geochemistry*. Springer, pp. pp. 271–309.
- Jørgensen, B.B., Parkes, R.J., 2010. Role of sulfate reduction and methane production by organic carbon degradation in eutrophic fjord sediments (Limfjorden, Denmark). *Limnol. Oceanogr.* 55 (3), 1338–1352.
- Jørgensen, B.B., Weber, A., Zopfi, J., 2001. Sulfate reduction and anaerobic methane oxidation in Black Sea sediments. *Deep-Sea Res. I Oceanogr. Res. Pap.* 48 (9), 2097–2120.
- Jørgensen, B.B., Bottcher, M.E., Luschen, H., Neretin, L.N., Volkov, I.I., 2004. Anaerobic methane oxidation and a deep H₂S sink generate isotopically heavy sulfides in Black Sea sediments. *Geochim. Cosmochim. Acta* 68 (9), 2095–2118.
- Kastner, M., Claypool, G., Robertson, G., 2008. Geochemical constraints on the origin of the pore fluids and gas hydrate distribution at Atwater Valley and Keathley canyon, northern Gulf of Mexico. *Mar. Pet. Geol.* 25 (9), 860–872.
- Kim, J.H., et al., 2016. Marine silicate weathering in the anoxic sediment of the Ulleung Basin: evidence and consequences. *Geochem. Geophys. Geosyst.* 17 (8), 3437–3453.
- Komada, T., et al., 2016. Organic matter cycling across the sulfate-methane transition zone of the Santa Barbara Basin, California borderland. *Geochim. Cosmochim. Acta* 176, 259–278.
- Kress, N., Herut, B., 2001. Spatial and seasonal evolution of dissolved oxygen and nutrients in the Southern Levantine Basin (Eastern Mediterranean Sea): chemical characterization of the water masses and inferences on the N : P ratios. *Deep-Sea Res. I Oceanogr. Res. Pap.* 48 (11), 2347–2372.
- Lettmann, K.A., et al., 2012. Estimation of biogeochemical rates from concentration profiles: a novel inverse method. *Estuar. Coast. Shelf Sci.* 100, 26–37.
- Leventhal, J., 1983. An interpretation of carbon and sulfur relationships in Black-Sea sediments as indicators of environments of deposition. *Geochim. Cosmochim. Acta* 47 (1), 133–137.
- Londry, K., Marais, D., 2003. Stable carbon isotope fractionation by sulfate-reducing bacteria. *Appl. Environ. Microbiol.* 69 (5), 2942–2949.
- Magalhães, V.H., et al., 2012. Formation processes of methane-derived authigenic carbonates from the Gulf of Cadiz. *Sediment. Geol.* 243, 155–168.
- Martens, C.S., Berner, R.A., 1977. Interstitial water chemistry of anoxic Long Island sound sediments. 1. Dissolved gases. *Limnol. Oceanogr.* 22 (1), 10–25.

- März, C., Hoffmann, J., Bleil, U., De Lange, G.J., Kasten, S., 2008. Diagenetic changes of magnetic and geochemical signals by anaerobic methane oxidation in sediments of the Zambezi deep-sea fan (SW Indian Ocean). *Mar. Geol.* 255 (3–4), 118–130.
- März, C., Riedinger, N., Sena, C., Kasten, S., 2018. Phosphorus dynamics around the sulphate-methane transition in continental margin sediments: Authigenic apatite and Fe (II) phosphates. *Mar. Geol.* 404, 84–96.
- Meister, P., Liu, B., Ferdelman, T., Jørgensen, B., Khalili, A., 2013. Control of sulphate and methane distributions in marine sediments by organic matter reactivity. *Geochim. Cosmochim. Acta* 104, 183–193.
- Milkov, A.V., 2004. Global estimates of hydrate-bound gas in marine sediments: how much is really out there? *Earth Sci. Rev.* 66 (3–4), 183–197.
- Milkov, A., Sassen, R., 2002. Economic geology of offshore gas hydrate accumulations and provinces. *Mar. Pet. Geol.* 19 (1), 1–11.
- Neretin, L.N., et al., 2004. Pyritization processes and greigite formation in the advancing sulfidization front in the upper Pleistocene sediments of the Black Sea. *Geochim. Cosmochim. Acta* 68 (9), 2081–2093.
- Niewohner, C., Hensen, C., Kasten, S., Zabel, M., Schulz, H.D., 1998. Deep sulfate reduction completely mediated by anaerobic methane oxidation in sediments of the upwelling area off Namibia. *Geochim. Cosmochim. Acta* 62 (3), 455–464.
- Pastor, L., et al., 2017. Early diagenesis in the sediments of the Congo deep-sea fan dominated by massive terrigenous deposits: part III - sulfate- and methane- based microbial processes. *Deep-Sea Res. II-Top. Stud. Oceanogr.* 142, 139–150.
- Paull, C., Normark, W., Ussler, W., Caress, D., Keaten, R., 2008. Association among active seafloor deformation, mound formation, and gas hydrate growth and accumulation within the seafloor of the Santa Monica Basin, offshore California. *Mar. Geol.* 250 (3–4), 258–275.
- Pierrot, D., Lewis, E., Wallace, D.W.R., 2006. MS Excel Program Developed for CO₂ System Calculations. Carbon Dioxide Information Analysis Center, Oak Ridge National Laboratory, Oak Ridge.
- Pohlman, J.W., Ruppel, C., Hutchinson, D.R., Downer, R., Coffin, R.B., 2008. Assessing sulfate reduction and methane cycling in a high salinity pore water system in the northern Gulf of Mexico. *Mar. Pet. Geol.* 25 (9), 942–951.
- Poulton, S., Canfield, D., 2005. Development of a sequential extraction procedure for iron: implications for iron partitioning in continentally derived particulates. *Chem. Geol.* 214 (3–4), 209–221.
- Reeburgh, W.S., 1976. Methane consumption in Cariaco trench waters and sediments. *Earth Planet. Sci. Lett.* 28 (3), 337–344.
- Reeburgh, W.S., 2007. Oceanic methane biogeochemistry. *Chem. Rev.* 107 (2), 486–513.
- Reimers, C., Rüttenberg, K., Canfield, D., Christiansen, M., Martin, J., 1996. Porewater pH and authigenic phases formed in the uppermost sediments of the Santa Barbara Basin. *Geochim. Cosmochim. Acta* 60 (21), 4037–4057.
- Rickard, D., Luther, G.W., 2007. Chemistry of iron sulfides. *Chem. Rev.* 107 (2), 514–562.
- Roy, H., Weber, H.S., Tarpgaard, I.H., Ferdelman, T.G., Jørgensen, B.B., 2014. Determination of dissimilatory sulfate reduction rates in marine sediment via radioactive S-35 tracer. *Limnol. Oceanogr. Methods* 12, 196–211.
- Sansone, F.J., Martens, C.S., 1981. Methane production from acetate and associated methane fluxes from anoxic coastal sediments. *Science* 211 (4483), 707–709.
- Sauvage, J., Spivack, A.J., Murray, R.W., D'Hondt, S., 2014. Determination of in situ dissolved inorganic carbon concentration and alkalinity for marine sedimentary porewater. *Chem. Geol.* 387, 66–73.
- Sayles, F.L., 1979. The composition and diagenesis of interstitial solutions—I. Fluxes across the seawater-sediment interface in the Atlantic Ocean. *Geochim. Cosmochim. Acta* 43 (4), 527–545.
- Sayles, F.L., Curry, W.B., 1988. Delta-C-13, TCO₂, and the metabolism of organic-carbon in deep-sea sediments. *Geochim. Cosmochim. Acta* 52 (12), 2963–2978.
- Sayles, F.L., Manheim, F.T., 1975. Interstitial solutions and diagenesis in deeply buried marine sediments - results from deep-sea drilling project. *Geochim. Cosmochim. Acta* 39 (2), 103–127.
- Scholz, F., Hensen, C., Schmidt, M., Geersen, J., 2013. Submarine weathering of silicate minerals and the extent of pore water freshening at active continental margins. *Geochim. Cosmochim. Acta* 100, 200–216.
- Schulz, H.D., 2006. Quantification of Early Diagenesis: Dissolved Constituents in Pore Water and Signals in the Solid Phase, Marine Geochemistry. Springer, Berlin, pp. 73–124.
- Sela-Adler, M., et al., 2015. Geochemical evidence for biogenic methane production and consumption in the shallow sediments of the SE Mediterranean shelf (Israel). *Cont. Shelf Res.* 101, 117–124.
- Sholkovitz, E., 1973. Interstitial water chemistry of Santa Barbara Basin sediments. *Geochim. Cosmochim. Acta* 37 (9), 2043–2073.
- Sivan, O., Schrag, D., Murray, R., 2007. Rates of methanogenesis and methanotrophy in deep-sea sediments. *Geobiology* 5 (2), 141–151.
- Snyder, G.T., et al., 2007. Pore water profiles and authigenic mineralization in shallow marine sediments above the methane-charged system on Umitaka spur, Japan Sea. *Deep-Sea Res. II-Top. Stud. Oceanogr.* 54 (11–13), 1216–1239.
- Stookey, L.L., 1970. Ferrozine - a new spectrophotometric reagent for iron. *Anal. Chem.* 42 (7), 779–781.
- Sun, X., Turchyn, A.V., 2014. Significant contribution of authigenic carbonate to marine carbon burial. *Nat. Geosci.* 7 (3), 201–204.
- Teal, L., Bulling, M.T., Parker, E., Solan, M., 2008. Global patterns of bioturbation intensity and mixed depth of marine soft sediments. *Aqua. Biol.* 2 (3), 207–218.
- Treude, T., Boetius, A., Knittel, K., Wallmann, K., Jørgensen, B.B., 2003. Anaerobic oxidation of methane above gas hydrates at hydrate ridge, NE Pacific Ocean. *Mar. Ecol. Prog. Ser.* 264, 1–14.
- Treude, T., et al., 2005. Anaerobic oxidation of methane and sulfate reduction along the Chilean continental margin. *Geochim. Cosmochim. Acta* 69 (11), 2767–2779.
- Treude, T., et al., 2014. Sulfate reduction and methane oxidation activity below the sulfate-methane transition zone in Alaskan Beaufort Sea continental margin sediments: implications for deep sulfur cycling. *Geochim. Cosmochim. Acta* 144, 217–237.
- Valentine, D.L., 2002. Biogeochemistry and microbial ecology of methane oxidation in anoxic environments: a review. *Anton. Leeuw. Int. J. Gen. Mol. Microbiol.* 81 (1–4), 271–282.
- Wallace, P.J., Dickens, G.R., Paull, C.K., Ussler, W., 2000. Effects of Core Retrieval and Degassing on the Carbon Isotope Composition of Methane in Gas Hydrate-and Free Gas-Bearing Sediments from the Blake Ridge. Proceedings of the Ocean Drilling Program. Scientific Results. Texas A&M University, pp. 101–112.
- Wallmann, K., et al., 2008. Silicate weathering in anoxic marine sediments. *Geochim. Cosmochim. Acta* 72 (12), 2895–2918.
- Whiticar, M.J., 1999. Carbon and hydrogen isotope systematics of bacterial formation and oxidation of methane. *Chem. Geol.* 161 (1–3), 291–314.
- Xu, Y.Y., Pierrot, D., Cai, W.J., 2017. Ocean carbonate system computation for anoxic waters using an updated CO₂SYS program. *Mar. Chem.* 195, 90–93.
- Yao, W.S., Millero, F.J., 1993. The rate of sulfide oxidation by delta-MnO₂ in seawater. *Geochim. Cosmochim. Acta* 57 (14), 3359–3365.
- Yao, W.S., Millero, F.J., 1996. Oxidation of hydrogen sulfide by hydrous Fe(III) oxides in seawater. *Mar. Chem.* 52 (1), 1–16.
- Zeebe, R.E., Wolf-Gladrow, D., 2001. CO₂ in Seawater: Equilibrium, Kinetics, Isotopes: Equilibrium, Kinetics, Isotopes. Elsevier.
- Zhang, C., Lanoil, B., 2004. Geomicrobiology and biogeochemistry of gas hydrates and cold seeps. *Chem. Geol.* (3–4), 187–194 ynnn.